A ROBUST COMPARISON APPROACH OF VELOCITY DATA BETWEEN MRI AND CFD BASED ON DIVERGENCE-FREE SPACE PROJECTION

Taha Sabri Koltukluoglu⋆ *Sven Hirsch*‡ *Christian Binter*♯ *Sebastian Kozerke*♯ *Gábor Székely*⋆ *Aymen Laadhari*⋆

⋆ Computer Vision Laboratory, Swiss Federal Institute of Technology, CH-8092 Zürich
♯ Institute for Biomedical Engineering, Swiss Federal Institute of Technology, CH-8092 Zürich
‡ Institute of Applied Simulation, Zurich University of Applied Sciences, CH-8820 Wädenswil

ABSTRACT

Recent achievements in 4D flow MRI increased the interest of CFD-MRI studies, which require comparison of velocity fields from both approaches for validation purposes. A novel flow regularization approach is proposed to provide a ground truth and to perform robust, mathematically reasonable comparisons between CFD and MRI. Our suggested method projects the measured and denoised data into the same space as the computational domain and applies the Helmholtz-Hodge theorem to recover the divergence-free property of the flow field by decomposing the velocity field into its divergence-free, curl-free and harmonic components. Furthermore, an aortic phantom study has been set-up under fully controlled laminar flow conditions with helical flow patterns to validate the proposed method using phase-contrast MRI measurements, whereas a dynamic stenosed case was used under turbulent flow conditions to analyse the robustness of applied pre-processings including the denoising of MRI data and the decomposition of velocity vector field.

1. INTRODUCTION

Recently, 4D flow MRI combining 3D spatial encoding with three-directional velocity-encoding has revealed great potential [1]. However, such measurements are limited by many factors such as acquisition times, signal-to-noise ratio and resolution depending on the set-up and region of interest. Numerical phantoms play an important role in the assessment and validation of hemodynamics. However, due to the different spatial representation of the vector fields between the image and computational domain, the validation is difficult. Although such combined studies are under extensive research, a reasonable comparison method has not yet been developed. Most of these works do either not describe in detail how the comparisons were achieved exactly or perform visual interpretation [2, 3, 4], whereas some other works compare velocity magnitude profiles and/or peak-velocities [5, 6], linear correlation coefficients [7] or volumetric flow rates [8]. Most of these comparisons are performed on 2D planes, do not define any norm or do not consider flow properties. Due to their limitations, such comparisons can often lead to misleading arguments. The presented work proposes the development of a divergence-free ground truth within the computational domain for numerical phantoms to achieve a meaningful comparison of computations and the measurements within the same space based on L^1, L^2 or L^∞ norms. These properties, to the author's best knowledge, have not been considered yet by any other combined CFD and MRI studies. Denoising is achieved by utilizing normalized median test [9]. The feasibility of the proposed approach is tested and validated using in-vitro experiments of an aortic phantom under laminar flow conditions with helical flow patterns. Furthermore, the applied pre-processings were analysed for their goodness using in-vitro experiments of a stenosed phantom under dynamic and turbulent conditions. The latter case has not been used for numerical computations.

2. EXPERIMENTAL SETTING

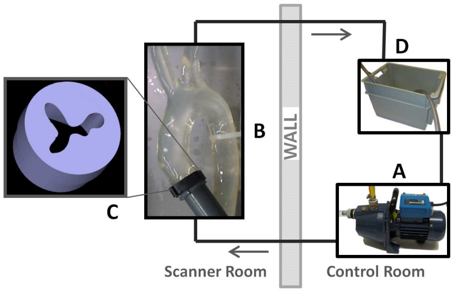

Fig. 1. Experimental phantom setup.

A silicon replica of a healthy human aortic arch (Elastrat, Switzerland) (B) was connected to a centrifugal pump (A) (BG-GP 636, Einhell Germany AG, Germany, maximum pressure 3.9 bar) via PVC tubing with 19 mm inner diameter with a total length of 20 m. Inlet and outlet were connected to a reservoir (D) resulting in an open circuit. A schematic of the setup can be seen in Fig. 1. The flow rate was controlled

---

This work was supported by the Swiss National Science Foundation grant 320030-149567.

using a ball bearing valve (C) placed 1.5 m downstream of the pump. Working fluid was H_2O with a temperature of $29°C$. The flow rate was monitored in 10 min intervals by Phase-Contrast MRI.

First, the flow was adopted in such a way, that the flow were static laminar under helical flow patterns without stenosis. Secondly, a rigid model of the aortic valve was designed using the valve orifice geometry of an aortic stenosis patient obtained by 2D MRI as a template. The orifice area was scaled to be 0.75 mm^2, and a cone shaped inlet was applied. This geometry was then 3D printed (Dimension Elite, Stratasys Ltd., Eden Prairie, MN, USA) using Acrylonitrile butadiene styrene (ABS) as a source material and used to obtain dynamic turbulent flow under stenosed condition. For the acquisition of the flow field a 3D spoiled Gradient-Echo sequence with flow encoding gradients was used. In order to achieve a higher velocity-to-noise ratio a Bayesian Multi-Point approach [10] with three different encoding velocities (280, 93 and 40 cm/s) per direction was chosen. Flip angle was set to 10 degrees, the voxel size was 1 mm isotropic with a field of view of 250 x 155 x 60 mm^3 and TE/TR were 5.9 ms and 10 ms, respectively. Total scan time was 15.5 min. All scans were performed using a 6-element cardiac coil on a 3T Philips scanner (Achieva, Philips Healthcare, Best, The Netherlands). Linear Phase Correction was applied to compensate for the eddy-current induced background phase.

3. PRE-PROCESSINGS OF THE NUMERICAL PHANTOM

Flow reconstruction yields both the proton density images and three-directional velocity data, denoted by $\boldsymbol{u}_{\text{MRI}}$. The phantom aorta was segmented semi-automatically with snake evolution methods using ITK-SNAP [11], see Fig. 2 (left). The surface mesh was smoothed with VMTK [12]. The mesh was built using *snappyHexMesh*, an OpenFOAM utility for creating hexahedral meshes.

3.1. Denoising of MRI data

The three-dimensional velocity data was composed with the segmentation binary mask, such that only the original values were kept within the surface of the segmented aorta. Values outside the surface were set to zero, such that they are not considered by the latter interpolation of measurements onto the mesh domain. After these processes, one is still left with the noise within the aorta, for which fast, accurate and automatic post-processings are required to get an appropriate input for numerical computations. Outlier detection techniques should also avoid heavy computational cost. This problem has been extensively studied in the existing literature [13]. We have applied the *normalized median test* proposed by [9]. In order to use the MRI acquisitions as initial conditions for the numerical simulations, the denoised data were projected onto the mesh domain using the linear interpolation provided by ITK [14]. The resulting projection of denoised velocities, denoted by $\bar{\boldsymbol{u}}_{\text{MRI}}$, does not respect the incompressibility constraint, and therefore a projection onto the divergence-free space were performed to address this issue.

3.2. Projection onto the divergence-free space

The Helmholtz-Hodge decomposition [15] is adopted. For regularity reasons, it is supposed that $\bar{\boldsymbol{u}}_{\text{MRI}}$ is quadratically integrable, and the aortic domain, Ω, is assumed to be a bounded, simply-connected and Lipschitz subdomain of $\mathbb{R}^3$. Under such assumptions, the following space splitting holds:

$$\left(L^2\left(\Omega\right)\right)^3 = \mathrm{H}_{\text{div},0}\left(\Omega\right) \oplus \mathrm{H}_{\text{curl},0}\left(\Omega\right) \oplus \mathrm{H}_{\text{har}}\left(\Omega\right),$$

where $\mathrm{H}_{\text{div},0}$ is the Sobolev space of square integrable vector fields with a square integrable divergence and a free-divergence , $\mathrm{H}_{\text{curl},0}$ is the Sobolev space of square integrable vectors with a square integrable curl and a free-curl , and H_{har} is the space of harmonic scalar functions $q \in \mathrm{H}^1(\Omega)$ having zero Laplacian. As a matter of fact, the vector $\bar{\boldsymbol{u}}_{\text{MRI}}$ can be uniquely decomposed into the sum $\bar{\boldsymbol{u}}_{\text{MRI}} = \tilde{\boldsymbol{u}} + \boldsymbol{u}_{\wedge} + \boldsymbol{u}^{\star}$, where $\tilde{\boldsymbol{u}} \in \mathrm{H}_{\text{div},0}\left(\Omega\right)$, $\boldsymbol{u}_{\wedge} \in \mathrm{H}_{\text{curl},0}\left(\Omega\right)$ and $\boldsymbol{u}^{\star} \in \mathrm{H}_{har}\left(\Omega\right)$. In what follows, we look for the divergence-free component of the denoised velocity, simply denoted by $\tilde{\boldsymbol{u}}^{\star} = \tilde{\boldsymbol{u}} + \boldsymbol{u}^{\star}$. Since the space $\mathrm{H}_{\text{curl},0}$ coincides with the gradient of potential space, it exists a potential $q \in \mathrm{H}_0^1(\Omega)$ such that $\boldsymbol{u}_{\wedge} = \nabla q$. Let us assume that $f = -\mathrm{div}\,\bar{\boldsymbol{u}}_{\text{MRI}} \in \mathrm{H}^{-1}(\Omega)$, where $\mathrm{H}^{-1}(\Omega)$ is the dual space of $\mathrm{H}_0^1(\Omega)$. We use no-slip boundary condition at the aortic wall Γ_5 to ensure the well-posedness of the problem, while homogeneous Neumann boundary condition is considered on the remaining boundaries. Let $\boldsymbol{n}$ denote the outward unit normal vector on the boundary. By applying the divergence operator, the projection problem reads

$$\mathscr{P}_{\perp} : \textit{find } \tilde{\boldsymbol{u}}^{\star} = \bar{\boldsymbol{u}}_{\mathit{MRI}} - \nabla q \in H_{\mathit{div}}(\Omega) \textit{ such that}$$

$$-\Delta q = f \text{ in } \Omega\,, \quad q = 0 \text{ on } \Gamma_5 \text{ and } \quad \nabla_{\boldsymbol{n}} q = 0 \text{ on } \partial\Omega \backslash \Gamma_5.$$

4. MATHEMATICAL MODEL

4.1. Navier-Stokes equations for Newtonian fluids

The flow is modelled as homogeneous, incompressible, and Newtonian fluid governed by the Navier-Stokes equations by solving the following steady state problem, $\mathscr{P}_{\text{fd}}$: *for* $T > 0$ *and* $t \in (0,T)$, *find* $\boldsymbol{u} \in \mathcal{C}^0\left((0,T), L^2(\Omega)^3\right) \cap L^2\left((0,T), \left(H_0^1(\Omega)\right)^3\right)$ *and* $p \in L^2\left((0,T), L_0^2(\Omega)\right)$ *such that*

$$\rho\left(\frac{\partial \mathbf{u}}{dt} + \boldsymbol{u} \cdot \nabla \boldsymbol{u}\right) - \mathbf{div}\,\boldsymbol{\sigma}(\boldsymbol{u}, p) = \mathbf{0} \quad \text{in } (0,T) \times \Omega$$

$$\mathrm{div}\,\boldsymbol{u} = 0 \quad \text{in } (0,T) \times \Omega$$

where $\boldsymbol{u}$, p are the computed velocity and pressure fields respectively, $\boldsymbol{\sigma}(\boldsymbol{u}, p)$ represents the Cauchy stress tensor,

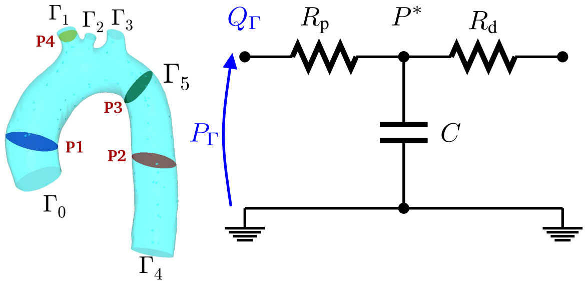

Fig. 2. Left: Nomenclature used for the boundaries and the cross-sectional planes through the aorta. Right: Schematic representation of the Windkessel model.

and the gravity is neglected. Being consistent with the experiment, corresponding parameters are used for water at $29°C$. These are $\rho = 10^3\,\mathrm{kg/m^3}$ for density and $\mu = 8.01 \cdot 10^{-4}\,\mathrm{kg/(sm)}$ for kinematic viscosity. To ensure that the problem $\mathscr{P}_\mathrm{fd}$ is well-posed, reasonable boundary conditions are required. The aortic wall is assumed to be rigid and a no-slip boundary condition is imposed on Γ_5, meaning that frictional forces will create a boundary layer along the wall. Post-processed and projected velocity data, $\tilde{\boldsymbol{u}}^\star$, is prescribed on the inlet, Γ_0. The remaining boundary conditions are modelled using multiscale couplings.

4.2. Multiscale coupling with zero-dimensional model

Reduced order modeling represent a useful formalism that can provide partial but accurate information about the arterial hemodynamics. During the past decades, there has been significant developments using several techniques of multiscale modeling, where reduced order models, also referred to as lumped-parameter models, are coupled with multidimensional description of the cardiovascular system [16]. Such reduced order models provide boundary conditions to be coupled with the detailed three-dimensional model. In this way, flow rate and pressure may be exchanged between the models of different complexity. In this work, a reduced circulation model allows to describe the systemic hemodynamics and provides a physiological pressure load at the downstream boundary of the descending aorta [17].

Among the existing models, the three-element Windkessel model is represented by an analog electrical circuit scheme, and it accounts for the vessel wall compliance and the fluid viscosity through a capacitor C and two resistances R_p and R_d, see Fig. 2. The following second order differential problem holds: $\mathscr{P}_{0d}$: *find* P_Γ *such that*

$$P_\Gamma - P^* + CR_d\frac{dP_\Gamma}{dt} = (R_1 + R_2)\,Q_\Gamma + CR_1R_2\frac{dQ_\Gamma}{dt}.$$

Using the flow rate Q_Γ provided by the fluid solver, i.e. $\mathscr{P}_\mathrm{fd}$, as input, the reduced model allows to get a physiological pressure load applied as boundary condition on the outlets Γ_i, $i \in \{1, 2, 3, 4\}$. The parameters of the reduced model are tuned in a dynamic case to obtain physiologically relevant results. In the presented work, the coupled problem is solved until the steady state, where a threshold tolerance ϵ is reached. Fig. 3 reveals the entire workflow.

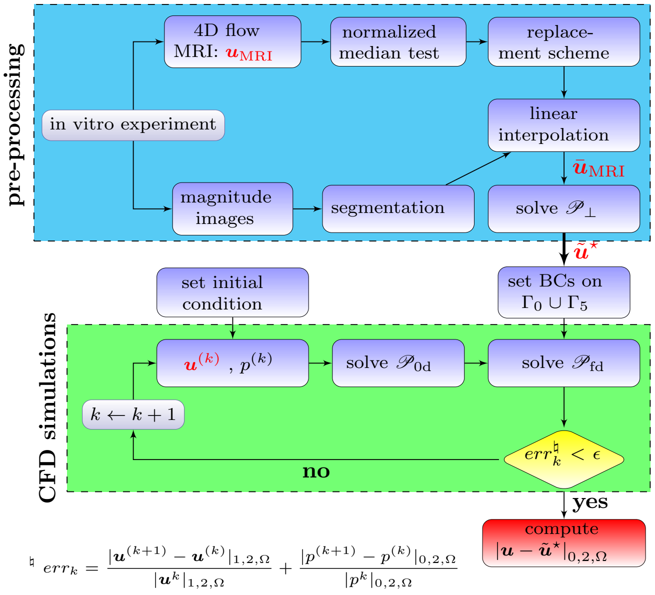

Fig. 3. Workflow: Pre-processing and simulation.

5. NUMERICAL EXAMPLES AND VALIDATION

The numerical phantom was implemented using icoFoam, an OpenFOAM [18] solver for incompressible, laminar Navier-Stokes equations using the PISO algorithm. The first experiment is concerned with numerical validation of the divergence-free projection. A validation case was implemented in 2D where the exact solution is known. The problem was solved with Rheolef [19] finite element framework and the error was compared between the computed and the exact solutions for several polynomial approximations. Let us consider the initial vector $\boldsymbol{u} = \tilde{\boldsymbol{u}} + \boldsymbol{u}_\wedge + \boldsymbol{u}^\star$ such that $\tilde{\boldsymbol{u}} = \left(\sin^2(2\pi x)\sin(4\pi y), -\sin^2(2\pi y)\sin(4\pi x)\right)^T$, $\boldsymbol{u}_\wedge = \left(2.2\sin(4\pi x)\sin^2(2\pi y), 2.2\sin(4\pi y)\sin^2(2\pi x)\right)^T$ and $\boldsymbol{u}^\star = \left(1.7\log\left(x^2+y^2\right), 1.7\log\left(x^2+y^2\right)\right)^T$. Given $\boldsymbol{u}$, this test consists in finding the divergence-free component $\tilde{\boldsymbol{u}}^\star = \tilde{\boldsymbol{u}} + \boldsymbol{u}^\star$. The spatial accuracy is studied by computing the error in L^2, denoted by $\|.\|_{0,2,\Omega}$, and L^∞, denoted by $\|.\|_{0,\infty,\Omega}$, norms with respect to the exact solution, respectively for several finite element polynomial approximations. By observing the slope in logarithmic scale, Fig. 4 depicts that the error evolution shows similar convergence rates to the expected theoretical errors. In particular, the L^2 error has a convergence rate equal to k when using $P_{k,k\geq 1}$ polynoms.

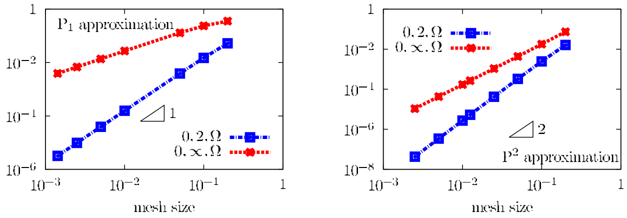

Fig. 4. Convergence properties of the div-free projection.

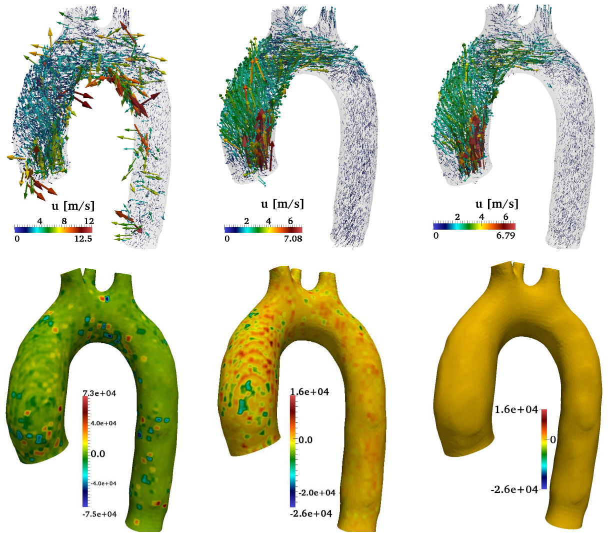

raw vector $\boldsymbol{u}_{\mathrm{MRI}}$ denoised vector $\tilde{\boldsymbol{u}}_{\mathrm{MRI}}$ divergence-free vector $\tilde{\boldsymbol{u}}^\star$

Fig. 5. Pre-processings shown under stenosed condition. Top: Velocity vector. Bottom: Divergence of the velocity.

Following the preprocessing steps described in Section 3, we perform the denoising and divergence-free projection in the case of a dynamic and stenotic phantom. Results in Fig. 5 clearly show the accuracy of the method under turbulent conditions, where the outliers are removed and the final velocity respects the incompressibility constraint. Notice that div $\tilde{\boldsymbol{u}}^\star < 0.05s^{-1}$.

In the second experiment, we performed numerical computations under laminar flow conditions with helical flow patterns using the denoised data as depicted in the graph in Section 4.2. Four defined planes are considered across the aorta, see Fig. 2(left), where a quantitative comparison of the velocity magnitude is performed. Comparisons in Fig. 6 show that the velocity magnitudes turned out to be almost identical in the defined planes P1, P2 and P3 across the aorta, see Fig. 2. However, a slight difference is observed in P4, which corresponds to the brachiocephalic artery. A potential explanation is that this error originates from the small lengths of the arches and from the low accuracy of the MRI acquisitions in these small arches. Moreover, the same observation holds when we evaluate the flow rates on the outlets. Unlike the flow rate on the descending aorta, Table 1 shows less similarities with respect to the experimental acquisitions in the arches. Therefore, the normalized error between the computed solution and the ground truth in the entire computational domain is $\int_\Omega |\boldsymbol{u} - \tilde{\boldsymbol{u}}^\star| / \int_\Omega |\tilde{\boldsymbol{u}}^\star| \approx 0.1129$.

Since the flow considered in the aorta has a helical pattern, see streamlines in Fig. 6, we chose the *helical flow index* (HFI) as an indicator to quantify the helicity [20]. HFI measures the alignment between the local velocity $\boldsymbol{u}$ and the vorticity $\boldsymbol{w}$ vectors, and it is given by the normalized helicity density $\mathrm{HFI} = \boldsymbol{u} \cdot \boldsymbol{w} / (|\boldsymbol{u}|\,|\boldsymbol{w}|)$. Accordingly, HFI is given by the cosine of the angle between $\boldsymbol{u}$ and $\boldsymbol{w}$. Therefore, HFI is close to 1 if the flow is purely helical, while the sign of HFI gives the direction of the rotation. The index is calculated on data and computational results, referred to as $\widetilde{\mathrm{HFI}}^\star$ and HFI respectively (see Fig. 6), and it shows the zones of almost purely helical flow where $|\mathrm{HFI}| \approx 1$.

	pre-processed data [m^3/s]	computations [m^3/s]
Γ_1	2.798×10^{-5}	5.409×10^{-5}
Γ_2	1.984×10^{-5}	3.362×10^{-5}
Γ_3	4.287×10^{-5}	5.512×10^{-5}
Γ_4	9.041×10^{-5}	8.322×10^{-5}

Table 1. Comparison between initial and computed fluxes.

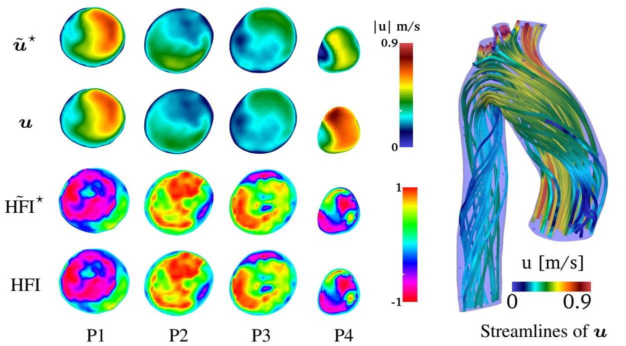

Fig. 6. Comparison between data and computations under laminar flow conditions.

6. CONCLUSION

A novel approach has been proposed to perform reliable comparisons between CFD and MRI. Phantom experiments of laminar flow under helical patterns have been performed. Numerical computations were compared against MRI acquisitions, and results show good agreement. As a future extension, the present strategies will be used to simulate a dynamic flow considering a stenotic valve upstream the domain using a blood mimicking flow instead of H_2O. Stability and the numerical issues will be provided in a forthcoming work.

7. REFERENCES

[1] M. Markl, A. Frydrychowicz, S. Kozerke, M. Hope, and O. Wieben, "4D flow MRI," *Magn. Reson. Im.*, vol. 36, no. 5, pp. 1015–1036.

[2] Y. Papaharilaou, D.J. Doorly, S.J. Sherwin, J.Peiro, J. Anderson, B. Sanghera, N. Watkins, and CG. Caro, "Combined mri and computational fluid dynamics detailed investigation of flow in a realistic coronary artery bypass graft model," *Proc. Intl. Soc. Mag. Reson.*, 2001.

[3] V.L. Rayzand, L. Boussel, G. Acevedo-Bolton, A. J. Martin, W.L.Young, M.T. Lawton, R. Higashida, and D. Saloner, "Numerical simulations of flow in cerebral aneurysms: comparison of cfd results and in vivo mri measurements," *J. Biomech. Eng.*, vol. 130, 2008.

[4] M. Midulla, R. Moreno, A. Baali, M. Chau, A. Negre-Salvayre, F. Nicoud, J.P. Pruvo, S. Haulon, and H. Rousseau, "Haemodynamic imaging of thoracic stent-grafts by computational fluid dynamics (cfd): presentation of a patient-specific method combining magnetic resonance imaging and numerical simulations," *Eur. Radiol.*, vol. 22, no. 10, pp. 2094–2102, 2012.

[5] T.I. Yiallourou, J.R. Kroeger, N. Stergiopulos, D. Maintz, B.A. Martin, and A.C. Bunck, "Comparison of 4D phase-contrast MRI flow measurements to computational fluid dynamics simulations of cerebrospinal fluid motion in the cervical spine," *PloS one*, vol. 7, no. 12, 2012.

[6] T.I. Yiallourou, L. Asboth, J. Kroeger, D. Maintz, A.C. Bunck, N. Stergiopulos, and B.A. Martin, "Quantitative comparison of 4D MRI flow measurements to 3D computational fluid dynamics simulation of cerebrospinal fluid movement in the spinal subarachnoid space," *10th international workshop on Biomedical Engineering*, pp. 1–4, 10 2011.

[7] Q. Long, X.Y. Xu, U. Köhler, M.B. Robertson, I.Marshall, and P.Hoskins, "Quantitative comparison of cfd predicted and mri measured velocity fields in a carotid bifurcation phantom," *Biorheology*, vol. 39, no. 3, pp. 467–474, 2002.

[8] J.P. Ku, C.J. Elkins, and C.A. Taylor, "Comparison of CFD and MRI flow and velocities in an in vitro large artery bypass graft model," *Ann. Biomed. Eng.*, vol. 33, no. 3, pp. 257–269, 2005.

[9] J. Westerweel and F. Scarano, "Universal outlier detection for PIV data," *Exp. Fluids.*, vol. 39, no. 6, pp. 1096–1100, 2005.

[10] C. Binter, V. Knobloch, R. Manka, A. Sigfridsson, and S. Kozerke, "Bayesian multipoint velocity encoding for concurrent flow and turbulence mapping," *Magn. Reson. Med.*, vol. 69, pp. 1337–1345, 2013.

[11] P.A. Yushkevich, J. Piven, H. C. Hazlett, R. G. Smith, S. Ho, J. C. Gee, and G. Gerig, "User-guided 3D active contour segmentation of anatomical structures: Significantly improved efficiency and reliability," *Neuroimage*, vol. 31, no. 3, pp. 1116–1128, 2006.

[12] L. Antiga, M. Piccinelli, L. Botti, B. Ene-Iordache, A. Remuzzi, and D.A. Steinman, "An image-based modeling framework for patient-specific computational hemodynamics," *Med. and Biolog. Eng. and Comp.*, vol. 46, no. 11, pp. 1097–1112, 2008.

[13] J. Ashburner and K.J.Friston, "Voxel-based morphometry - the methods," *Neuroimage*, vol. 11, pp. 805–821, 2000.

[14] H. J. Johnson, M. McCormick, L. Ibáñez, and The Insight Software Consortium, *The ITK Software Guide*, Kitware Inc., third edition, 2013, *In press*.

[15] F. Maria Denaro, "On the application of the helmholtz-hodge decomposition in projection methods for incompressible flows with general boundary conditions," *Int. J. Numer. Meth. Fluids*, vol. 46, pp. 43–69, 2003.

[16] F.N. Van de Vosse, "Mathematical modelling of the cardiovascular system," *J. Eng. Math.*, vol. 47, no. 3-4, pp. 175–183, 2003.

[17] J.P. Murgo, N. Westerhof, J.P. Giolma, and S.A. Altobelli, "Aortic input impedance in normal man: relationship to pressure wave forms," *Circulation*, vol. 62, pp. 105–116, 1980.

[18] H. G. Weller, G. Tabor, H. Jasak, and C. Fureby, "A tensorial approach to computational continuum mechanics using object-oriented techniques," *Comput. Phys.*, vol. 12, no. 6, pp. 620–631, nov 1998.

[19] P. Saramito, *Efficient C++ finite element computing with Rheolef*, CNRS-CCSD ed., 2013.

[20] R. Lorenz, J. Bock, A.J. Barker, F. von Knobelsdorff-Brenkenhoff, W. Wallis, J.G. Korvink, M.M. Bissell, J. Schulz-Menger, and M. Markl, "4D flow magnetic resonance imaging in bicuspid aortic valve disease demonstrates altered distribution of aortic blood flow helicity," *Magn. Reson. Med.*, vol. 71, no. 4, pp. 1542–1553, 2014.